Acta Mech 227, 581–599 (2016)
DOI 10.1007/s00707-015-1479-z

ORIGINAL PAPER

Benedict Thomas · Tarapada Roy

Vibration analysis of functionally graded carbon nanotube-reinforced composite shell structures

Received: 11 July 2015 / Revised: 17 September 2015 / Published online: 16 October 2015

Abstract This article deals with the vibration analysis of functionally graded carbon nanotube-reinforced composite (FG-CNTRC) shell structures. The material properties of an FG-CNTRC shell are graded smoothly through the thickness direction of the shell according to uniform distribution and some other functionally graded (FG) distributions (such as FG-X, FG-V, FG-O and FG-Λ) of the volume fraction of the carbon nanotube (CNT), and the effective material properties are estimated by employing the extended rule of mixture. An eight-noded shell element considering transverse shear effect according to Mindlin's hypothesis has been employed for the finite element modelling and analysis of the composite shell structures. The formulation of the shell midsurface in an arbitrary curvilinear coordinate system based on the tensorial notation is also presented. The Rayleigh damping model has been implemented in order to study the effects of carbon nanotubes (CNTs) on the damping capacity of such shell structures. Different types of shell panels have been analyzed in order to study the impulse and frequency responses. The influences of CNT volume fraction, CNT distribution, geometry of the shell and material distributions on the dynamic behavior of FG-CNTRC shell structures have also been presented and discussed. Various types of FG-CNTRC shell structures (such as spherical, ellipsoidal, doubly curved and cylindrical) have been analyzed and discussed in order to compare studies in terms of settling time, first resonant frequency and absolute amplitude corresponding to first resonant frequency based on the impulse and frequency responses, and the effects of CNTs on vibration responses of such shell structures are also presented. The results show that the CNT distribution and volume fraction of CNT have a significant effect on vibration and damping characteristics of the structure.

List of symbols

V_{cnt}, V_{m}	Carbon nanotube and matrix volume fraction
E_{11}^{cnt} and E_{22}^{cnt}	Young's moduli of CNT in longitudinal and transverse directions
G_{12}^{cnt}	Shear modulus of CNT
E_{m} and G_{m}	Young's moduli and shear modulus of the isotropic matrix
η_1, η_2 and η_3	CNT efficiency parameters
$\upsilon_{12}^{\text{cnt}}$ and υ_{m}	Poisson's ratio of CNT and matrix
h	Thickness
nd	Number of nodes in an element

B. Thomas · T. Roy (✉)
Department of Mechanical Engineering, National Institute of Technology, Rourkela,
Rourkela, Odisha 769008, India
E-mail: tarapada@nitrkl.ac.in

N_i	Shape function corresponding to the i node
α_1, α_2	Curvilinear coordinates
u_{0i}, v_{0i} and w_{0i}	Deflection of midsurface at ith node in α_1, α_2 and z directions
θ_{1i}, θ_{2i}	Rotation of normal at ith node about α_2 axis and α_1 axis, respectively
ε^0_{xx}, ε^0_{yy} and γ^0_{xy}	In-plane strains of the midsurface in the Cartesian coordinate system
k_{xx}, k_{yy} and k_{xy}	Bending strains (curvatures) of the midsurface in the Cartesian coordinates system
A_{ij}, B_{ij}, D_{ij} and A^s_{ij}	Extensional, flexural-extensional coupling, bending and transverse shear stiffness, respectively

1 Introduction

Composite shell structures are very important structural components as they support applied external forces efficiently by virtue of their special geometrical shape. Such structures are widely used in numerous fields such as civil, architectural, aeronautical and marine engineering and are frequently subjected to dynamic loads that cause vibrations. So the study of vibration is an important facet in the successful application of these structures.

Functionally graded materials (FGMs) are a new breed of composites that have a smooth and continuous variation of material properties from one surface to another which in turn helps to mitigate the stress concentrations found in laminated composites. The concept of FGM can be efficiently utilized for better management of material's microstructure in a plate/shell structure reinforced by CNTs to achieve improved vibrational behavior. The addition of CNT with functionally graded material (FGM) provides enriched mechanical, electrical as well as thermal properties with an additional advantage of attaining desired properties by varying the distribution and composition of CNTs.

From a technological point of view, nanostructured materials have shown the prospective to become the new generation material due to their high levels of performance and multifunctionality. Carbon nanotubes (CNTs) and their composites have fascinated many researchers to work in this area because of their superior mechanical, thermal and electrical properties. Compared with the conventional CFRP, carbon nanotube-reinforced composites (CNTRCs) have the potential of significantly better strength and stiffness. Among the major properties exhibited by nanocomposites, their unique ability to absorb vibrations turns out to be one of the most important features in view of numerous applications in distinct fields of engineering such as aerospace, automotive and civil engineering. The ability to absorb and dissipate mechanical energy, normally referred to as damping capacity, has become an essential feature for multifunctional composite structures.

After the discovery of carbon nanotubes by Iijima [1], most studies have focused on the material properties of carbon nanotube-reinforced composites [2,3]. Thermo-mechanical properties of epoxy-based nanocomposites based on low-weight fraction of randomly oriented single- and multiwalled CNTs were investigated by Fidelus et al. [4]. Using molecular dynamic simulation, Han and Elliott [5] obtained the elastic modulus of composite structures under CNT reinforcement and investigated the effect of volume fraction of SWNTs on mechanical properties of nanocomposites. Zhu et al. [6] revealed that the addition of a small amount of carbon nanotube in the matrix can considerably improve the mechanical, electrical and thermal properties of a polymeric composites. Odegard et al. [7] have presented a technique for developing constitutive models for polymer composite systems reinforced with single-walled carbon nanotubes (SWCNTs). Dong-Li Shi et al. [8] obtained the elastic properties of a CNT-reinforced composite for aligned and randomly oriented CNT by micromechanics method to account for nanotube waviness and agglomeration. The waviness and agglomeration result in reduction of the stiffness of the material. Wuite and Adali [9] examined the deflection and stress of nanocomposite-reinforced beams using a multiscale analysis. They found that a small percentage of nanotube reinforcement leads to significant improvements in beam stiffness.

Shen et al. [10] used the idea of FGM to the nanocomposites to investigate thermal buckling and post-buckling behavior of CNTRC plates. By using the concept of FGM, Shen [11,12] suggested that the interfacial bonding strength can be improved by the use of a graded distribution of CNTs in the matrix and studied the nonlinear bending behavior of simply supported, functionally graded nanocomposite plates reinforced by SWNTs subjected to a transverse uniform or sinusoidal load in thermal environment. Zhu et al. [13] presented bending and free vibration analyses of thin-to-moderately thick composite plates reinforced by SWCNTs using the finite element method. Vibrational properties of functionally graded nanocomposite beams reinforced by randomly oriented straight SWCNTs under the action of moving load were presented by Yas and Heshmati [14]. Based on the Eshelby–Mori–Tanaka approach, Aragh et al. [15] presented the vibrational behavior of continuously graded carbon nanotube-reinforced cylindrical panels. Moradi-Dastjerdi et al. [16]

reported the effect of nanotube aspect ratio on the free vibration characteristics of a functionally graded nanocomposite cylinder reinforced by wavy single-walled carbon nanotubes (CNTs) based on a mesh-free method. In recent times, several research works have been carried out on functionally graded carbon nanotube-reinforced composites considering various types of distribution (uniform and functionally graded distribution). Flexural strength and free vibration of FG-CNTRC cylindrical panels have been analyzed by Zhang et al. [17] considering four types of distributions of uniaxial aligned reinforcements by using the mesh-free kp-Ritz method. Liew et al. [18] identified and highlighted topics relevant to FG-CNTRC and reviewed the recent research works that have been reported in these topics and also explored the possibility of future work in this area. Zhang et al. [19–21] extended the element-free IMLS-Ritz method to obtain approximate solutions for the free vibration of various types of moderately thick FG-CNTRC skew plates and triangular plates reinforced by single-walled carbon nanotubes (SWCNTs). They have also presented the buckling solution of an FG-CNT-reinforced composite thick skew plate. Phung-Van et al. [22] presented a simple and effective formulation based on isogeometric analysis (IGA) and higher-order shear deformation theory (HSDT) to investigate the static and dynamic behavior of functionally graded carbon nanotube-reinforced composite plates. Alibeigloo and Emtehani [23] presented the elasticity solution of an FG-CNTRC plate for free vibration and the bending behavior of an FG-CNTRC rectangular plate subjected to uniform pressure with different edges boundary condition by using the differential quadrature method (DQM) along in-plane coordinates and state-space analytical approach in transverse direction. Recently, Kundalwal and Meguid [24] investigated the effects of carbon nanotube (CNT) waviness on the active constrained layer damping (ACLD) of the laminated hybrid composite shells. Zeighampour et al. [25] derived the governing equations of the conical shell by using the first-order shear deformable shell model.

Weng [26] predicted the effective bulk moduli, and the underlying elastic fields of a particle and a fiber-reinforced composite whose matrix properties were graded linearly along the radial distance by means of change of the dependent variable. Alian et al. [27] developed a multiscale modelling technique to determine the effective elastic moduli of CNT-reinforced epoxy composites containing either well-dispersed or agglomerated carbon nanotubes (CNTs) by employing MD simulations and the Mori–Tanaka method. Kumar and Ray [28] investigated active damping of geometrically nonlinear vibrations of doubly curved smart sandwich shells integrated with a patch of active constrained layer damping (ACLD) treatment. The constraining layer of the ACLD treatment was made of the vertically/obliquely reinforced 1–3 piezoelectric composites (PZCs). Kundalwal et al. [29] studied the damping characteristics of smart laminated continuous fuzzy fiber-reinforced composite (FFRC) shells integrated with the patches of ACLD treatment. The study revealed that the damping characteristics of these structures can be improved significantly by using 1–3 piezoelectric composites (PZCs).

The aim of the present work is the vibration analysis of a carbon nanotube-based functionally graded composite shell structure. It involves the mathematical modelling of material properties, finite element modelling and analysis of various types of composite shell structures and the effects of CNTs on the vibration characteristics (viz. settling time, resonant frequencies and absolute amplitudes of vibration) of such shell structures. An eight-noded shell finite element has been formulated in a curvilinear coordinate system based on Mindlin's hypothesis. The formulation of the shell midsurface in an arbitrary curvilinear coordinate system based on the tensorial notation is also presented. Various types of FG-CNTRC shell structures (such as spherical, ellipsoidal, doubly curved and cylindrical) have been analyzed and discussed based on the impulse and frequency responses in order to study the effects of CNTs on vibration responses of such structures. After validating the formulation, the influence of CNT volume fraction, CNT distribution, geometry of the shell structure and material distributions on the vibration behavior of such shell structures is investigated. It is observed that the addition of CNTs and CNT distribution has a significant influence on the elastic properties as well as on the vibration behavior of such a structure.

2 Modelling of material properties

It is assumed that the FG-CNTRC shell structure is made from a mixture of isotropic matrix (epoxy resin) and fibers (CNTs), and the material properties are assumed to be graded along the thickness direction according to linear distributions (UD, FG-X, FG-V, FG-O and FG-Λ) of the volume fraction of carbon nanotubes.

2.1 Linear material distribution

In order to examine the effect of different distributions of the CNT on the dynamic behavior of the FG-CNTRC shell, uniform distribution (UD) and functionally graded distributions (FG-X, FG-V, FG-O and FG-Λ) of

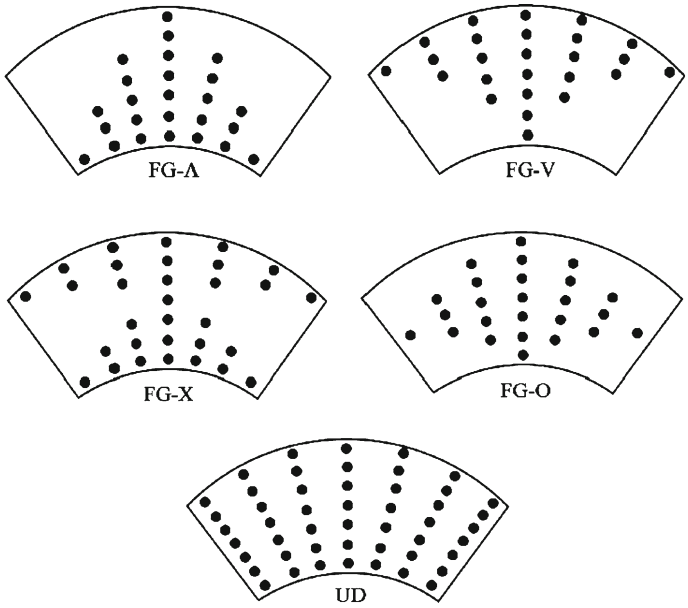

Fig. 1 Configurations of various CNTRC spherical shells

carbon nanotubes along the thickness direction of the nanocomposite shell are considered as in Fig. 1. The CNT volume fractions V_{cnt} of various types of the FG-CNTRC beam can be expressed as:

$$V_{\text{cnt}} = \begin{cases} V_{\text{cnt}}^{*} & \text{(UD CNTRC)}, \\ \left(1 - \frac{2|z|}{h}\right) V_{\text{cnt}}^{*} & \text{(FG-V CNTRC)}, \\ \frac{4|z|}{h} V_{\text{cnt}}^{*} & \text{(FG-X CNTRC)}, \\ 2\left(1 - \frac{2|z|}{h}\right) V_{\text{cnt}}^{*} & \text{(FG-O CNTRC)}, \\ \left(1 + \frac{2z}{h}\right) V_{\text{cnt}}^{*} & \text{(FG-}\Lambda\text{ CNTRC)}. \end{cases} \tag{1}$$

Here, V_{cnt}^{*} depends on density and mass fractions of both matrix and CNT,

$$V_{\text{cnt}}^{*} = \frac{w_{\text{cnt}}}{w_{\text{cnt}} + \frac{\rho_{\text{cnt}}}{\rho_m} - \left(\frac{\rho_{\text{cnt}}}{\rho_m}\right) w_{\text{cnt}}}, \tag{2}$$

where w_{cnt} is the mass fraction of the nanotube and ρ_{cnt} and ρ_m are the densities of carbon nanotube and matrix, respectively. For this linear material property variation, material properties can be obtained by substituting the value of V_{cnt} in Eq. (1).

2.2 Extended rule of mixture

To determine the effective material properties of the CNTRC shell the extended rule of mixture is employed, which can be expressed as [11]

$$\begin{aligned} E_{11} &= \eta_1 V_{\text{cnt}} E_{11}^{\text{cnt}} + V_m E_m, \\ \frac{\eta_2}{E_{22}} &= \frac{V_{\text{cnt}}}{E_{22}^{cnt}} + \frac{V_m}{E_m}, \\ \frac{\eta_3}{G_{12}} &= \frac{V_{\text{cnt}}}{G_{12}^{cnt}} + \frac{V_m}{G_m}. \end{aligned} \tag{3}$$

Since Poisson's ratio depends weakly on the position, we assume υ_{12} to be:

$$\upsilon_{12} = V_{\text{cnt}}^{*} \upsilon_{12}^{\text{cnt}} + V_m \upsilon_m.$$

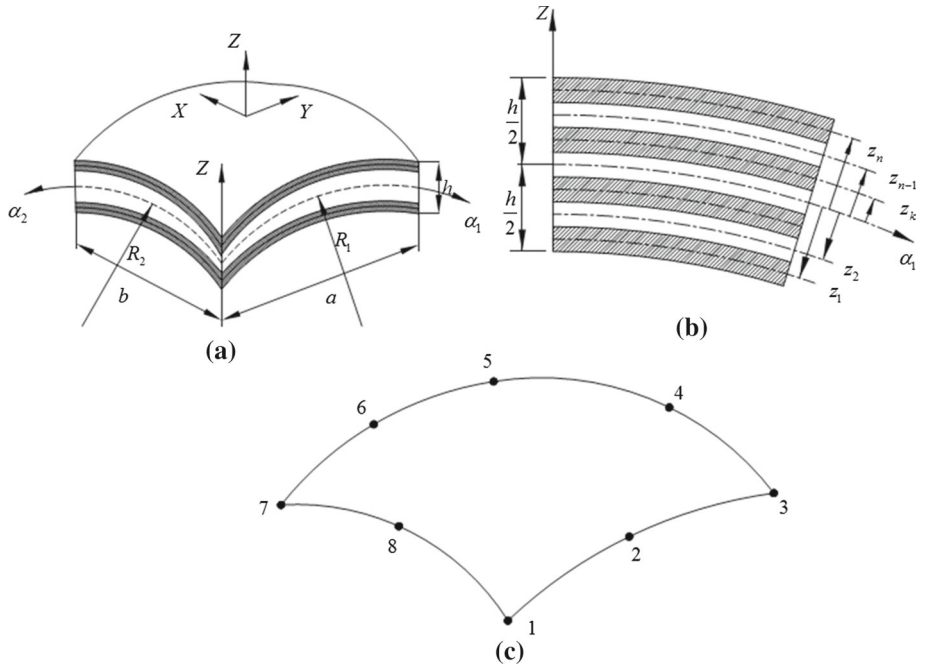

Fig. 2 **a** Geometry of shell structure in Cartesian coordinates, **b** coordinate system of laminate and **c** eight-noded shell element

2.3 Finite Element formulation and analysis of FG-CNTRC shell structure

The stress-resultant-type Koiter's shell theory [30] has been considered in the present finite element (FE) formulation of the composite shell structures. The effect of shear deformation to Koiter shell theory based on Mindlin's hypothesis [31,32] has also been considered in the present FE formulation.

2.3.1 Geometry of midsurface

The shell geometry used in the present formulation has been developed using a curvilinear coordinate system with the midplane of the shell assumed to be the reference surface as shown in Fig. 2a. The normal direction coordinate to the middle surface of the shell has been represented by z. A set of parametric equations can be defined in the following form:

$$X = X(\alpha_1, \alpha_2); \quad Y = Y(\alpha_1, \alpha_2); \quad Z = Z(\alpha_1, \alpha_2)$$

where (α_1, α_2) are two independent coordinates in the parametric space of the midsurface curvilinear coordinates of the shell. The reference surface or the shell midsurface can be described in the global Cartesian coordinates in terms of the position vector as

$$r(\alpha_1, \alpha_2) = X(\alpha_1, \alpha_2)\,\hat{i} + Y(\alpha_1, \alpha_2)\,\hat{j} + Z(\alpha_1, \alpha_2)\,\hat{k} \tag{4}$$

where $\hat{i}$, $\hat{j}$ and $\hat{k}$ are unit vectors along the X, Y and Z axis, respectively.

The tangent vectors to the coordinate curves at a point can be represented as the basis vectors

$$r_{,1} = \frac{\partial r}{\partial \alpha_1}, \quad \text{and} \quad r_{,2} = \frac{\partial r}{\partial \alpha_2}. \tag{5}$$

Letting $(X, Y, Z) = (x^1, x^2, x^3)$ and $(\alpha_1, \alpha_2) = (u^1, u^2)$, the position $(\vec{r})$ and tangent $(\vec{E}_\alpha)$ vectors can be written in the form of summation as follows:

$$\vec{r} = \vec{r}(u^1, u^2) = x^i(\mathrm{u}^1, \mathrm{u}^2)\hat{e}_i, \quad \vec{E}_\alpha = \frac{\partial \vec{r}}{\partial u^\alpha} = \frac{\partial x^i}{\partial u^\alpha}\hat{\mathrm{e}}_i, \ \alpha = 1, 2. \tag{6}$$

The unit normal vector to the tangent plane of any point on the reference surface can be expressed as

$$\hat{e}_n = \hat{n}(\alpha_1, \alpha_2) = \frac{\vec{E}_1 \times \vec{E}_2}{\left|\vec{E}_1 \times \vec{E}_2\right|} = \frac{r_1 \times r_{,2}}{|r_1 \times r_2|}. \tag{7}$$

The scalar product of a vector joining two points on the middle surface (α_1, α_2) and $(\alpha_1 + \mathrm{d}\alpha_1, \alpha_2 + \mathrm{d}\alpha_2)$ is given as

$$\mathrm{d}s^2 = \mathrm{d}\vec{r} \cdot \mathrm{d}\vec{r} = (r_{,1}\mathrm{d}\alpha_1 + r_{,2}\mathrm{d}\alpha_2) \cdot (r_{,1}\mathrm{d}\alpha_1 + r_{,2}\mathrm{d}\alpha_2) = \frac{\partial \vec{r}}{\partial u^\alpha} \cdot \frac{\partial \vec{r}}{\partial u^\beta} \mathrm{d}u^\alpha \mathrm{d}u^\beta = a_{\alpha\beta}\mathrm{d}u^\alpha \mathrm{d}u^\beta \tag{8}$$

where $a_{\alpha\beta} = \frac{\partial \vec{r}}{\partial u^\alpha} \cdot \frac{\partial \vec{r}}{\partial u^\beta} = \frac{\partial x^i}{\partial u^\alpha}\frac{\partial x^i}{\partial u^\beta}$ with $\alpha, \beta = 1, 2$ is called two-dimensional surface metric tensor. The scalar product of the arc length on the shell midsurface can also be written in the quadratic form (i.e., called first fundamental form of surface) as

$$\begin{aligned} \mathrm{d}s^2 &= r_{,1} \cdot r_{,1}(\mathrm{d}\alpha_1)^2 + 2r_{,1} \cdot r_{,2}\mathrm{d}\alpha_1\mathrm{d}\alpha_2 + r_{,2} \cdot r_{,2}(\mathrm{d}\alpha_2)^2 \\ &= A_1^2(\mathrm{d}\alpha_1)^2 + 2A_{12}\mathrm{d}\alpha_1\mathrm{d}\alpha_2 + A_2^2(\mathrm{d}\alpha_2)^2 \\ &= a_{11}(\mathrm{d}\alpha_1)^2 + 2a_{12}\mathrm{d}\alpha_1\mathrm{d}\alpha_2 + a_{22}(\mathrm{d}\alpha_2)^2. \end{aligned} \tag{9}$$

The conjugate metric tensor $(a^{\alpha\beta})$ is defined such that $a^{\alpha\beta}a_{\beta\gamma} = \delta^\alpha_\gamma$, where δ^α_γ is the Kronecker delta. A point is considered on the shell midsurface with the unit normal vector $(\hat{n})$ at this point. The unit tangent vector $(\hat{T})$ to the curve which lies in the tangent plane to the surface of that point can be written as

$$\hat{T} = \frac{\mathrm{d}\vec{r}}{\mathrm{d}s}. \tag{10}$$

The curvature vector at the point of consideration can be expressed as

$$\vec{K} = \frac{\mathrm{d}\vec{r}}{\mathrm{d}s}. \tag{11}$$

A unit vector on the surface which is perpendicular to both the surface tangent vector $(\hat{T})$ and surface normal vector $(\hat{n})$ can be written as

$$\hat{u} = \hat{n} \times \hat{T} \tag{12}$$

where T^i, u^i and n^i form a right-handed system. The curvature vector $(\vec{K})$ in the component form can be written as

$$\vec{K} = \frac{\mathrm{d}\hat{T}}{\mathrm{d}s} = k_{(\mathrm{nor})}\hat{n} + k_{(\mathrm{geo})}\hat{u} = \vec{K}_n + \vec{K}_g \tag{13}$$

where $k_{(\mathrm{nor})}$ and $k_{(\mathrm{geo})}$ are called normal and geodesic curvatures, respectively. The normal curvature can be determined as follows:

$$\begin{aligned} k_{(\mathrm{nor})} &= -\hat{T} \cdot \frac{\mathrm{d}\hat{n}}{\mathrm{d}s} = -\frac{\mathrm{d}\vec{r}}{\mathrm{d}s} \cdot \frac{\mathrm{d}\hat{n}}{\mathrm{d}s} \\ &\Rightarrow k_{(\mathrm{nor})}\mathrm{d}s^2 = -\mathrm{d}\vec{r} \cdot \mathrm{d}\hat{n} = e(\mathrm{d}u^1)^2 + 2f\mathrm{d}u^1\mathrm{d}u^2 + g(\mathrm{d}u^2)^2 \\ &= b_{11}(\mathrm{d}u^1)^2 + 2b_{12}\mathrm{d}u^1\mathrm{d}u^2 + b_{22}(\mathrm{d}u^2)^2 \\ &= b_{\alpha\beta}\mathrm{d}u^\alpha\mathrm{d}u^\beta \end{aligned} \tag{14}$$

where $b_{\alpha\beta} = -\frac{\partial \vec{r}}{\partial u^\alpha} \cdot \frac{\partial \hat{n}}{\partial u^\beta}$ with $\alpha, \beta = 1, 2$ is called the curvature tensor and $b_{\alpha\gamma}b_{\alpha\beta} = b^\gamma_\beta$ is called an associated curvature tensor. The normal curvature can also be expressed as

$$k_{(\mathrm{nor})} = \frac{b_{\alpha\beta}\mathrm{d}u^\alpha\mathrm{d}u^\beta}{\mathrm{d}s^2} = \frac{b_{\alpha\beta}\mathrm{d}u^\alpha\mathrm{d}u^\beta}{a_{\alpha\beta}\mathrm{d}u^\alpha\mathrm{d}u^\beta}. \tag{15}$$

The principals' curvatures $k_{(\mathrm{nor}1)}$ and $k_{(\mathrm{nor}2)}$ are the eigenvalues of the matrix with elements of $b^\gamma_\beta = b_{\alpha\gamma}b_{\alpha\beta}$.

So, the characteristic equation for the eigenvalue problem can be written as

$$(\mathrm{b}_{\alpha\beta} - k_{(\mathrm{nor})}a_{\alpha\beta})\lambda^{\alpha}\lambda^{\beta} = 0. \tag{16}$$

The maximum and minimum normal curvatures can be determined in those directions λ^{α},

$$(b_{\alpha\beta} - k_{(\mathrm{nor})}a_{\alpha\beta})\lambda^{\alpha} = 0. \tag{17}$$

Therefore, $k_{(nor)}$ must satisfy the following determinant:

$$\begin{aligned} &\left|(b_{\alpha\beta} - k_{(\mathrm{nor})}a_{\alpha\beta})\right| = 0, \\ &\Rightarrow k^2_{(\mathrm{nor})} - b_{\alpha\beta}a^{\alpha\beta}k_{(\mathrm{nor})} + \tfrac{(b_{11}b_{22}-b_{12}b_{21})}{(a_{11}a_{22}-a_{12}a_{21})} = 0, \\ &\Rightarrow k^2_{(\mathrm{nor})} - (k_{(\mathrm{nor1})} + k_{(\mathrm{nor2})})k_{(\mathrm{nor})} + k_{(\mathrm{nor1})}k_{(\mathrm{nor2})} = 0 \end{aligned} \tag{18}$$

where $k_{(\mathrm{nor1})}, k_{(\mathrm{nor2})}$ is the total or Gaussian curvature and $\frac{1}{2}(k_{(\mathrm{nor1})} + k_{(\mathrm{nor2})})$ is a mean curvature which are invariants. For an orthogonal curvilinear coordinate system, the surface metric tensor $(a_{\alpha\beta})$ and curvature tensor $(b_{\alpha\beta})$ can be written as given by Wempner and Talaslidis [33]

$$a_{\alpha\beta} = \begin{cases} a_{\alpha\alpha} & \text{if } \alpha = \beta \\ 0 & \text{if } \alpha \neq \beta \end{cases} \quad \text{and} \quad b_{\alpha\beta} = \begin{cases} b_{\alpha\alpha} & \text{if } \alpha = \beta \\ 0 & \text{if } \alpha \neq \beta \end{cases}. \tag{19}$$

The normal curvatures of the shell midsurface in orthogonal curvilinear coordinates can be expressed using Eqs. (9) and (15) as

$$\frac{1}{R_1} = \frac{b_{11}}{a_{11}} = -\frac{\hat{\mathrm{e}}_n.r_{,11}}{A_1^2} \text{ and } \frac{1}{R_2} = \frac{b_{22}}{a_{22}} = -\frac{\hat{\mathrm{e}}_n.r_{22}}{A_2^2} \tag{20}$$

where $A_1 = \sqrt{r_{,1}.r_1}$ and $A_2 = \sqrt{r_{,2}.r_{,2}}$ are the Lamé parameters, and the twist curvatures of the shell midsurface can be obtained as

$$\frac{1}{R_{12}} = -\frac{\hat{e}_n.r_{,12}}{A_1A_2}. \tag{21}$$

2.3.2 Isoparametric mapping

Figure 3 shows how Cartesian coordinates are converted into curvilinear coordinates, and it is again mapped into isoparametric form. The curvilinear coordinates (α_1, α_2) of any point within an element may be represented as

$$\alpha_1 = \sum_{i=1}^{\mathrm{nd}} N_i\alpha_{1i}; \quad \alpha_2 = \sum_{i=1}^{\mathrm{nd}} N_i\alpha_{2i}. \tag{22}$$

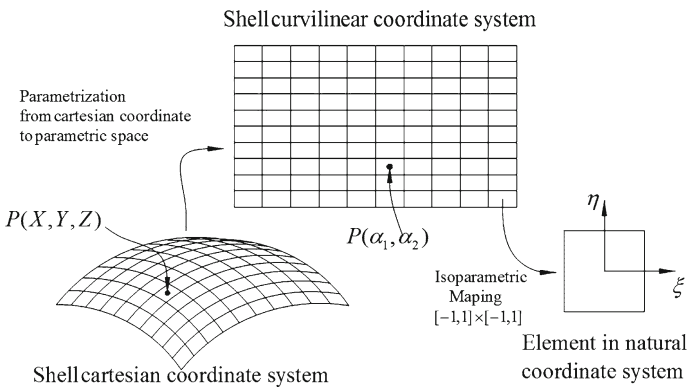

Fig. 3 Mapping of coordinates

The displacement components on the shell midsurface of any element can be given by

$$\left\{ u_0 \; v_0 \; w \; \theta_1 \; \theta_2 \right\}^{\mathrm{T}} = \sum_{i=1}^{\mathrm{nd}} N_i \left\{ u_{0i} \; v_{0i} \; w_i \; \theta_{1i} \; \theta_{2i} \right\}^{\mathrm{T}}. \tag{23}$$

In the present analysis, shape functions of an eight-node serendipity element are used which are given in the "Appendix".

2.3.3 Strain–displacement relations

Neglecting the normal strain component in the thickness direction, the five strain components of a doubly curved shell may be expressed as

$$\left[\varepsilon_{xx} \; \varepsilon_{yy} \; \gamma_{xy} \; \gamma_{yz} \; \gamma_{xz} \right]^{\mathrm{T}} = \left[\varepsilon^0_{xx} \; \varepsilon^0_{yy} \; \gamma^0_{xy} \; \gamma^0_{yz} \; \gamma^0_{xz} \right]^{\mathrm{T}} + z \left[k_{xx} \; k_{yy} \; k_{xy} \; 0 \; 0 \right]^{\mathrm{T}}. \tag{24}$$

The in-plane and transverse strain–displacement relations may be derived based on the present formulation and Koiter's shell theory [30].

In-plane/bending strain–displacement matrix

The strain components on the midsurface of the shell element are

$$\{\varepsilon\} = \left[\varepsilon^0_{xx} \; \varepsilon^0_{yy} \; \gamma^0_{xy} \; k_{xx} \; k_{yy} \; k_{xy} \right]^{\mathrm{T}}. \tag{25}$$

By using an isoparametric eight-noded shell element shown in Fig. 2c, the displacement component on the shell midsurface at any point within an element can be expressed as

$$\left\{ u_0 \; v_0 \; w \; \theta_1 \; \theta_2 \right\}^{\mathrm{T}} = [N] \left\{ d^e \right\}. \tag{26}$$

The midsurface strains and curvatures from Koiter's shell theory are:

$$\varepsilon^0_{xx} = \frac{1}{A_1}\frac{\partial u}{\partial \alpha_1} + \frac{v}{A_1 A_2}\frac{\partial A_1}{\partial \alpha_2} + \frac{w}{R_1}, \tag{27}$$

$$\varepsilon^0_{yy} = \frac{1}{A_2}\frac{\partial v}{\partial \alpha_2} + \frac{u}{A_1 A_2}\frac{\partial A_2}{\partial \alpha_1} + \frac{w}{R_2}, \tag{28}$$

$$\gamma^0_{xy} = \frac{1}{A_1}\frac{\partial v}{\partial \alpha_1} + \frac{1}{A_2}\frac{\partial u}{\partial \alpha_2} - \frac{u}{A_1 A_2}\frac{\partial A_1}{\partial \alpha_2} - \frac{v}{A_1 A_2}\frac{\partial A_2}{\partial \alpha_1} + \frac{2w}{R_{12}}, \tag{29}$$

$$k_{yy} = \frac{1}{A_2}\frac{\partial \theta_2}{\partial \alpha_2} + \frac{\theta_1}{A_1 A_2}\frac{\partial A_2}{\partial \alpha_1} - \frac{1}{2R_{12}}\left(\frac{1}{A_1}\frac{\partial v}{\partial \alpha_1} - \frac{1}{A_2}\frac{\partial u}{\partial \alpha_2} - \frac{u}{A_1 A_2}\frac{\partial A_1}{\partial \alpha_2} + \frac{v}{A_1 A_2}\frac{\partial A_2}{\partial \alpha_1} \right), \tag{30}$$

$$k_{xy} = \begin{bmatrix} \frac{1}{A_1}\frac{\partial \theta_2}{\partial \alpha_1} + \frac{1}{A_2}\frac{\partial \theta_1}{\partial \alpha_2} - \frac{\theta_1}{A_1 A_2}\frac{\partial A_1}{\partial \alpha_2} - \frac{\theta_2}{A_1 A_2}\frac{\partial A_2}{\partial \alpha_1} - \\ \frac{1}{2}\left(\frac{1}{R_1} - \frac{1}{R_2}\right)\left(\frac{1}{A_1}\frac{\partial v}{\partial \alpha_1} - \frac{1}{A_2}\frac{\partial u}{\partial \alpha_2} - \frac{u}{A_1 A_2}\frac{\partial A_1}{\partial \alpha_2} + \frac{v}{A_1 A_2}\frac{\partial A_2}{\partial \alpha_1}\right) \end{bmatrix}. \tag{31}$$

By using eight-noded isoparametric shape functions for Eq. (25), the strain components at any point on the shell midsurface can be expressed as

$$\{\varepsilon\} = \sum_{i=1}^{8} \begin{bmatrix} \frac{1}{A_1}\frac{\partial N_i}{\partial \alpha_1} & \frac{N_i}{A_1 A_2}\frac{\partial A_1}{\partial \alpha_2} & \frac{N_i}{R_1} & 0 & 0 \\ \frac{N_i}{A_1 A_2}\frac{\partial A_2}{\partial \alpha_1} & \frac{1}{A_2}\frac{\partial N_i}{\partial \alpha_2} & \frac{N_i}{R_2} & 0 & 0 \\ \frac{1}{A_2}\frac{\partial N_i}{\partial \alpha_2} - \frac{N_i}{A_1 A_2}\frac{\partial A_1}{\partial \alpha_2} & \frac{1}{A_1}\frac{\partial N_i}{\partial \alpha_1} - \frac{N_i}{A_1 A_2}\frac{\partial A_2}{\partial \alpha_1} & \frac{2N_i}{R_{12}} & 0 & 0 \\ -\frac{1}{2}\frac{1}{R_{12}}\left(\frac{1}{A_2}\frac{\partial N_i}{\partial \alpha_2} + \frac{N_i}{A_1 A_2}\frac{\partial A_1}{\partial \alpha_2}\right) & \frac{1}{2}\frac{1}{R_{12}}\left(\frac{1}{A_1}\frac{\partial N_i}{\partial \alpha_1} + \frac{N_i}{A_1 A_2}\frac{\partial A_2}{\partial \alpha_1}\right) & 0 & \frac{1}{A_1}\frac{\partial N_i}{\partial \alpha_1} & \frac{N_i}{A_1 A_2}\frac{\partial A_1}{\partial \alpha_2} \\ \frac{1}{2}\frac{1}{R_{12}}\left(\frac{1}{A_2}\frac{\partial N_i}{\partial \alpha_2} + \frac{N_i}{A_1 A_2}\frac{\partial A_1}{\partial \alpha_2}\right) & -\frac{1}{2}\frac{1}{R_{12}}\left(\frac{1}{A_1}\frac{\partial N_i}{\partial \alpha_1} + \frac{N_i}{A_1 A_2}\frac{\partial A_2}{\partial \alpha_1}\right) & 0 & \frac{N_i}{A_1 A_2}\frac{\partial A_2}{\partial \alpha_1} & \frac{1}{A_2}\frac{\partial N_i}{\partial \alpha_2} \\ C_0\left(\frac{1}{A_2}\frac{\partial N_i}{\partial \alpha_2} + \frac{N_i}{A_1 A_2}\frac{\partial A_1}{\partial \alpha_2}\right) & -C_0\left(\frac{1}{A_1}\frac{\partial N_i}{\partial \alpha_1} + \frac{N_i}{A_1 A_2}\frac{\partial A_2}{\partial \alpha_1}\right) & 0 & \frac{1}{A_2}\frac{\partial N_i}{\partial \alpha_2} - \frac{N_i}{A_1 A_2}\frac{\partial A_1}{\partial \alpha_2} & \frac{1}{A_1}\frac{\partial N_i}{\partial \alpha_1} - \frac{N_i}{A_1 A_2}\frac{\partial A_2}{\partial \alpha_1} \end{bmatrix} \begin{Bmatrix} u_{0i} \\ v_{0i} \\ w_i \\ \theta_{1i} \\ \theta_{2i} \end{Bmatrix},$$

$$\{\varepsilon\} = \left[B^e_b\right] \left\{ d^e \right\}. \tag{32}$$

$\left[B^e_b\right]$ is the element in-plane strain–displacement matrix, and $C_o = \frac{1}{2}\left(\frac{1}{R_1} - \frac{1}{R_2}\right)$.

2.3.4 Transverse strain–displacement matrix

The transverse shear strain vector of a doubly curved shell element based on FSDT can be represented as

$$\begin{Bmatrix} \gamma_{yz} \\ \gamma_{xz} \end{Bmatrix} = \begin{Bmatrix} \theta_2 + \frac{1}{A_2}\frac{\partial w}{\partial \alpha_2} - \frac{u}{R_{12}} - \frac{v}{R_2} \\ \theta_1 + \frac{1}{A_1}\frac{\partial w}{\partial \alpha_1} - \frac{u}{R_1} - \frac{v}{R_{12}} \end{Bmatrix}. \tag{33}$$

Also the transverse shear strain at any point on the shell midsurface can be represented as

$$\begin{Bmatrix} \gamma_{yz} \\ \gamma_{xz} \end{Bmatrix} = \sum_{k=1}^{\mathrm{nd}} \begin{bmatrix} -\frac{N_i}{R_{12}} & -\frac{N_i}{R_2} & \frac{1}{A_2}\frac{\partial N_i}{\partial \alpha_2} & 0 & N_i \\ -\frac{N_i}{R_1} & -\frac{N_i}{R_{12}} & \frac{1}{A_1}\frac{\partial N_i}{\partial \alpha_1} & N_i & 0 \end{bmatrix} \begin{Bmatrix} u_{0i} \\ v_{0i} \\ w_i \\ \theta_{1i} \\ \theta_{2i} \end{Bmatrix}, \tag{34}$$

$$\begin{Bmatrix} \gamma_{yz} \\ \gamma_{xz} \end{Bmatrix} = \left[B_s^e\right]\left\{d^e\right\}. \tag{35}$$

$\left[B_s^e\right]$ is the element transverse strain–displacement matrix.

2.3.5 Equation of motion

The dynamic finite element formulation has been derived by using Hamilton's principle after solving the energy expression, and the equation of motion can be written as

$$\left[M_{uu}^e\right]\left\{\ddot{d}^e\right\} + \left[K_{uu}^e\right]\left\{d^e\right\} = \left\{F^e\right\}. \tag{36}$$

Equation (36) is the dynamic finite element equation of one element.

Element Mass matrix

The element mass matrix can be expressed as:

$$[M_e] = \int_{-1}^{1}\int_{-1}^{1} [N]^{\mathrm{T}}[\rho][N]\,|J|\,\mathrm{d}\xi\,\mathrm{d}\eta \tag{37}$$

where $[\rho]$ and $[N]$ are density and shape function matrix, respectively, which are given in the 'Appendix.'

The final form of the elemental mass matrix can be expressed as

$$\left[M_{uu}^e\right] = \int_{-1}^{1}\int_{-1}^{1}\int_{-h/2}^{h/2} \rho\,[N]^{\mathrm{T}}[N]\,\mathrm{d}z\,|J|\,\mathrm{d}\xi\,\mathrm{d}\eta. \tag{38}$$

$\left[K_{uu}^e\right]$ is the element structural stiffness matrix which is given by

$$\left[K_{uu}^e\right] = \int_V \left[B_u^e\right]^{\mathrm{T}}[C]\left[B_u^e\right]\mathrm{d}V \tag{39}$$

where $\left[K_{uu}^e\right] = \left[K_{bb}^e\right] + \left[K_{ss}^e\right]$ and the matrices $\left[B_u^e\right]$ and $[C]$ are presented in the 'Appendix.'

The elements of ABD can be determined from the following integral forms:

$$\begin{pmatrix} A_{ij} & B_{ij} & D_{ij} \end{pmatrix} = \int_{-\frac{h}{2}}^{+\frac{h}{2}} \left(1 z z^2\right)\overline{Q_{ij}}\,\mathrm{d}z,\ \left(A_{ij}^s\right) = \int_{-\frac{h}{2}}^{+\frac{h}{2}} k_s\,\overline{Q_{ij}}\,\mathrm{d}z.$$

The shear correction factor of out-of-plane shears is denoted by k_s (taken as 5/6 for the present analysis). The shell structure is divided into 'n' number of layers in thickness direction as shown in Fig. 2b in order to determine the elements of ABD matrix,

$$A_{ij} = \sum_{k=1}^{n} \left(\overline{Q_{ij}}\right)_k (z_k - z_{k-1}),$$
$$B_{ij} = \frac{1}{2} \sum_{k=1}^{n} \left(\overline{Q_{ij}}\right)_k \left(z_k^2 - z_{k-1}^2\right), \quad \text{Here,} \quad i = 1, 3 \quad \text{and} \quad j = 1,\ 3$$
$$D_{ij} = \frac{1}{3} \sum_{k=1}^{n} \left(\overline{Q_{ij}}\right)_k \left(z_k^3 - z_{k-1}^3\right),$$

$\left(\overline{Q_{ij}}\right)_k$ is a transformed stiffness matrix at the midpoint of each layer which is a function of volume fraction of carbon fiber, ply angle, and power law index and $B_{ij} \neq 0$ due to material asymmetry.

$\left[K_{bb}^e\right]$ is the element in-plane/bending stiffness matrix.

$$\left[K_{bb}^e\right] = \int_V \left[B_b^e\right]^{\mathrm{T}} D_b \left[B_b^e\right] \mathrm{d}V,$$
$$\left[K_{bb}^e\right] = \int_\Omega \left[B_b^e\right]^{\mathrm{T}} \begin{bmatrix} A & B \\ B & D \end{bmatrix} \left[B_b^e\right] \mathrm{d}\Omega. \tag{40}$$

$\left[K_{ss}^e\right]$ is the element transverse shear stiffness matrix,

$$\left[K_{ss}^e\right] = \int_V \left[B_s^e\right]^{\mathrm{T}} D_s \left[B_s^e\right] \mathrm{d}V,$$
$$\left[K_{ss}^e\right] = \int_\Omega \left[B_s^e\right]^{\mathrm{T}} \left[\overline{D_s}\right] \left[B_s^e\right] \mathrm{d}\Omega, \tag{41}$$

$\{F^e\}$ is the element external mechanical force vector

$$\left\{F^e\right\} = \int_A [N]^{\mathrm{T}} \left\{f_s^e(x, y)\right\} \mathrm{d}A. \tag{42}$$

Damping in large systems can be modelled using Rayleigh damping or proportional damping and can be calculated as given by Chowdhury and Dasgupta [34] for a large degree of freedom system. Here the $[C]$ matrix is found such that

$$\{X\}^{\mathrm{T}} [C] \{X\} = \begin{bmatrix} \alpha + \beta\omega_1^2 & 0 & \cdots & 0 \\ 0 & \alpha + \beta\omega_2^2 & \ddots & \vdots \\ \vdots & \ddots & \ddots & 0 \\ 0 & \cdots & 0 & \alpha + \beta\omega_N^2 \end{bmatrix} = \begin{bmatrix} 2\xi_1\omega_1 & 0 & \cdots & 0 \\ 0 & 2\xi_2\omega_2 & \ddots & \vdots \\ \vdots & \ddots & \ddots & 0 \\ 0 & \cdots & 0 & 2\xi_N\omega_N \end{bmatrix} \tag{43}$$

where $\{X\}$ is the eigenvector of the system and α and β are the coefficients to be determined for N simultaneous equations.

$$\xi_i = \frac{\alpha}{2\omega_i} + \frac{\beta\omega_i}{2}. \tag{44}$$

ω_i and ξ_i are ith modal natural frequency and damping ratio, respectively. For any linear system, only few modes are enough to study its overall dynamics, so in the present study first 3 % of the total modes are taken as significant mode and 2.5 times of the chosen modes (and beyond the significant modes) are used. The damping

ratio of the first and last significant mode is taken as 0.01 and 0.03, respectively, after which all the damping ratios are either interpolated or extrapolated depending on their sequence as follows:

$$\xi_i = \frac{\xi_m - \xi_1}{\omega_m - \omega_1}(\omega_i - \omega_1) + \xi_1; \quad 1 \le i \le m,$$
$$\xi_i = \frac{\xi_m - \xi_1}{\omega_m - \omega_1}(\omega_{m+i} - \omega_1) + \xi_1; \quad m \le i \le 2.5m. \tag{45}$$

After assembly of elemental matrices, the equation of motion of whole structure can be represented as

$$[M]\left\{\ddot{d}\right\} + [C]\left\{\dot{d}\right\} + [K]\{d\} = \{F\}. \tag{46}$$

2.4 Frequency response analysis

A frequency response analysis is also carried out. In Eq. (42) if $\{F\}$ takes the form $\{F_0\}\,e^{i\omega t}$, $\{d\}$ is likely to take the form $\{d_0\}\,e^{i\omega t}$, where F_0, ω, d_0 are the amplitude of excitation force, exciting frequency and displacement vector achievable due to the excitation, respectively. The frequency-dependent responses can be obtained as

$$|\{d\}| = \left|\left[-[M]\,\omega^2 + i\,[C]\,\omega + [K]\right]^{-1}\{F_0\}\right|. \tag{47}$$

3 Results and discussion

Based on the finite element formulation, a computer code has been developed for the vibration analysis of FG-CNTRC shell structures. The non-dimensional central deflection and non-dimensional fundamental frequency of simply supported laminated spherical shells are obtained from the present code which are presented in Tables 1 and 2. It has been observed from Tables 1 and 2 that results are in excellent agreement with already published results [31,32]. After validation, various results are presented for vibration analysis of a functionally graded carbon nanotube-reinforced composite (FG-CNTRC) shell structure. Transient and frequency response analysis of different types of FG-CNTRC simply supported shell structures (i.e., spherical, ellipsoidal, doubly curved and cylindrical) is carried out to investigate the effects of some of the important parameters.

Table 1 Comparison of non-dimensional frequency

Ply orientation	a/h	R/a							
		Source	1	2	5	10	20	50	100	500
[0/90]	10	Present	13.834	10.4314	9.1644	8.96641	8.91575	8.89989	8.89488	8.87028
		Refs. [31,32]	14.481	10.749	9.2302	8.9841	8.9212	8.9035	8.9009	8.9001
	100	Present	124.21	67.3348	28.811	16.6965	11.8366	10.0591	9.77558	9.65602
		Refs. [31,32]	125.93	67.369	28.826	16.706	11.841	10.063	9.7825	9.6873
$[0/90]_s$	10	Present	14.3219	12.8041	12.3229	12.251	12.2326	12.2264	12.2238	12.2083
		Refs. [31,32]	16.172	13.447	12.437	12.28	12.24	12.229	12.228	12.226
	100	Present	124.056	68.0219	30.9927	20.347	16.627	15.4223	15.2405	15.1662
		Refs. [31,32]	126.33	68.294	31.079	20.38	16.638	15.426	15.245	15.184

For simply supported laminated spherical shells under uniformly distributed load

Table 2 Comparison of non-dimensional central deflection

Ply orientation	a/h	R/a							
		Source	1	2	5	10	20	50	100	500
[0/90]	10	Present	6.18987	13.3927	18.1998	19.1372	19.3846	19.4548	19.4648	19.4681
		Refs. [31,32]	6.054	12.668	17.994	19.069	19.365	19.452	19.464	19.469
	100	Present	0.06893	0.28439	1.75376	5.54788	11.2796	15.7164	16.6452	16.9657
		Refs. [31,32]	0.0718	0.2855	1.7535	5.5428	11.273	15.714	16.645	16.98
$[0/90]_s$	10	Present	5.82537	8.85739	10.0072	10.1884	10.2345	10.2474	10.2493	10.2499
		Refs. [31,32]	4.8366	8.0517	9.8249	10.141	10.222	10.245	10.249	10.251
	100	Present	0.0694	0.28527	1.54422	3.73305	5.6687	6.61625	6.77747	6.8307
		Refs. [31,32]	0.0715	0.2844	1.5358	3.7208	5.6618	6.6148	6.7772	6.8331

For simply supported laminated spherical shells under uniformly distributed load

3.1 Material properties of FG-CNTRC

A mathematical modelling for material properties is carried out in order to determine the mechanical properties of the FG composite laminates. First of all, the effective material properties of a FG-CNTRC shell are determined. Poly {(*m*-phenylenevinylene)-co-[(2,5-dioctoxy-*p*-phenylene) vinylene]}, referred as PmPV, is considered as the matrix in the present work, and the material properties of the matrix are considered as $E^m = 2.1$ GPa, $\nu^m = 0.34$ and $\rho^m = 1150$ kg/m^3 [21]. Han and Elliott [5] have selected a low value of Young's modulus, as those of Odegard et al. [7], for (10,10) SWCNTs assuming the effective thickness of CNTs to be 0.34 nm or more. As reported recently, the effective thickness of SWCNTs should be smaller than 0.142 nm to satisfy the Vodenitcharova–Zhang criterion [35]. Therefore, all material properties and effective thickness of SWCNTs used for the present analysis are properly selected according to the MD simulation results of Shen and Zhang [10]. So, considering (10, 10) SWCNTs for reinforcement, their material properties at $T = 300$ K (room temperature) associated with the effective wall thickness ($h = 0.067$ nm) are considered to be as follows [10]:

$$E_{11}^{\text{cnt}} = 5.64665 \text{ GPa}, \quad E_{22}^{\text{cnt}} = 7.0800 \text{ GPa}, \quad G_{12}^{\text{cnt}} = 1.9445 \text{ GPa}, \quad \nu_{12}^{\text{cnt}} = 0.175, \quad \rho^{\text{cnt}} = 1400 \text{ kg/m}^3.$$

The CNT efficiency parameters appearing in Eq. (3) are evaluated by matching the Young's moduli E_{11}^{cnt}, E_{22}^{cnt} and shear modulus G_{12}^{cnt} of CNTRCs obtained from the extended rule of mixture to ones predicted from MD simulations in [5]. For three values of nanotube volume fractions, the values of η_1, η_2 and η_3 are given in Table 3. As there are no MD results available for shear modulus G_{12} in [5] so presently it is assumed that $\eta_2 = \eta_3$ and $G_{23} = G_{13} = G_{12}$ [11]. Finally, the extended rule of mixture is employed to obtain the effective material properties of the FG-CNTRC shell. The volume fraction of carbon nanotubes is graded using uniform distribution (UD) and functionally graded distributions (FG-X, FG-V, FG-O and FG-Λ) along the thickness of the shell. Figure 4 shows the variation of the carbon nanotube volume fraction along the thickness of the shell for various CNT distributions. It is also observed that the obtained material properties follow the corresponding trends of CNT distributions (such as UD, FG-X, FG-V, FG-O and FG-Λ).

After determining the material properties, finite element modelling of the spherical shell was carried out by dividing it into 100 elements. After finite element modelling of the shell structure, impulse and frequency response analysis for a sixteen-layered laminate is performed. The analysis has been carried out by varying

Table 3 Comparison of Young's moduli for PmPV/CNT composite reinforced by SWCNT (10, 10) at $T_0 = 300$ K

V_{cnt}	MD [5]		Rule of mixture [21]			
	E_{11} (Gpa)	E_{22} (Gpa)	E_{11} (Gpa)	η_1	E_{22}(Gpa)	η_2
0.11	94.8	2.2	94.57	0.149	2.2	0.934
0.14	120.2	2.3	120.09	0.150	2.3	0.941
0.17	145.6	3.5	145.08	0.149	3.5	1.381

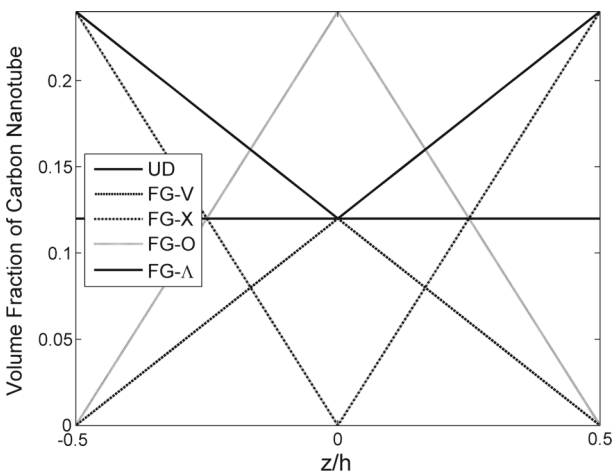

Fig. 4 Variation of CNT volume fraction through the thickness of shell for various CNT distributions

Table 4 Parameters and their variations used for the analysis

Parameters	Variations
SWCNT volume fraction (%age)	11, 14, 17
CNT distribution	UD, FG-V, FG-X, FG-O and FG-Λ
a/h	10, 100
R/a	1, 2, 5, 10, 50,100, 500

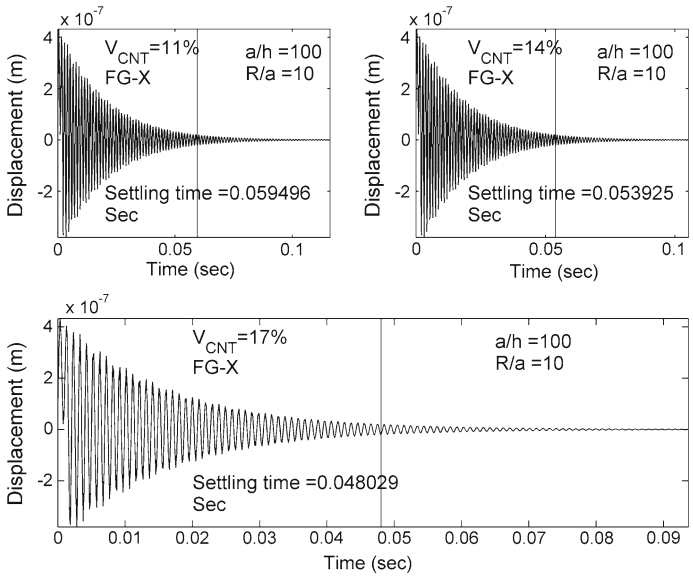

Fig. 5 Transient response of system due to impulse load for spherical shell with FG-X distribution

four parameters, namely SWCNT volume fraction, CNT distribution, a/h, and R/a as mentioned in Table 4. The results for impulse and frequency responses of an FG-CNTRC spherical shell are presented in Sects. 3.2 and 3.3, and a comparative study is also carried out for other types of shells which is described in Sect. 3.4.

3.2 Transient responses due to impulse loading

Impulse loading is applied at middle node in transverse direction, and a constant load 10 N is applied up to 10 time steps. Then, the transient response due to the load is obtained by the Duhamel integration technique, as any kind of vibration can be described as weighted combination of all possible fundamental modes for a linear system. The response in global coordinate is obtained by using the most significant mode. A parameter (i.e., settling time) is used in this present work for a comparative study of vibration damping. For the present study, the settling time is taken as the time at which the amplitude of response of vibration settles to 5 % of the maximum amplitude.

Figure 5 shows the transient responses of the spherical shell structure due to impulse load for an FG-X-type distribution considering different CNT volume fractions. It is evident from Fig. 5 that as the volume fraction of CNT increases the settling time decreases. So it is obvious from Fig. 5 that due to the addition of CNTs an increase in the damping capacity of the FG-CNTRC shell can be achieved. Figure 6 represents the effects of CNT volume fractions and shell geometry on the settling time (i.e., damping) of the thin shell spherical structure for FG-X distribution. In Fig. 6, the settling time increases rapidly for deep shell region and then becomes constant for a shallow shell and plate. Figure 6 also depicts that as the CNT volume fraction increases, the settling time decreases quickly which shows that CNTs have prominent effect on the settling time and hence on the damping. Figure 7 represents the effects of CNT distributions and shell geometry on the settling time of the thin spherical shell structure for 11 % CNT volume fraction. In Fig. 7, the settling time increases rapidly for the deep shell region and then becomes constant for the shallow shell and plate region for all types of CNT distributions. It is also observed from Fig. 7 that the FG-V distribution has the highest settling time and the

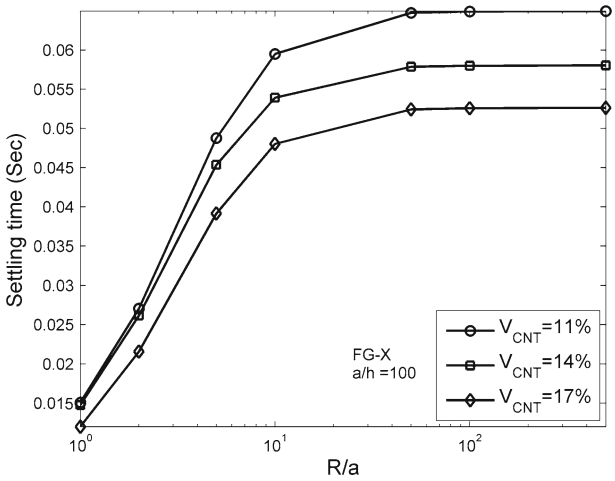

Fig. 6 Settling time with R/a ratio considering $a/h = 100$ and FG-X distribution for different CNT volume fractions

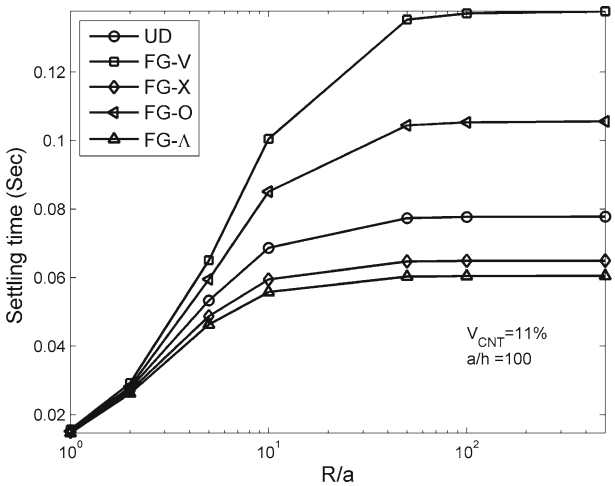

Fig. 7 Settling time with R/a ratio considering $a/h = 100$ and $V_{\text{cnt}} = 11\,\%$ for different CNT distributions

FG-Λ distribution has the lowest settling time. It is also clearly observed from Figs. 5, 6 and 7 that the settling time decreases with inclusions of CNTs, and the best CNT distribution is FG-Λ which gives the least settling time compared to the other CNT distributions considered.

3.3 Frequency response analysis of FG-CNTRC shell structures

A frequency response analysis has been carried out in order to study the effects of CNTs on the absolute transverse displacements of the midpoint of the shell and resonant frequencies. A concentrated load with an amplitude of 10 N is applied at the midnode in the transverse direction in order to perform frequency response based on Eq. (47) for various volume fractions of CNT.

Figure 8 depicts the frequency response of the spherical shell structure for different values of CNT volume fractions for a certain geometry (thick and deep); i.e., $R/a = 5$ and $a/h = 10$. It is clearly observed from Fig. 8 that there are clear variations in each curve, peak value of each curve and corresponding frequency of excitation (corresponding to the damped natural frequency) for a certain value CNT volume fraction. Figure 8 also reveals that as the volume fraction of CNT increases from 11 to 17 % the absolute amplitude decreases, whereas the corresponding resonant frequency increases. A similar trend is observed in Fig. 9 for various CNT distributions; the absolute amplitude follows a decreasing trend for all types of distribution, and it is more prominent in case of FG $-$ Λ-type distribution where a minimum value of absolute amplitude and maximum value of corresponding resonant frequency are observed. Figure 10 shows the variation of absolute amplitude

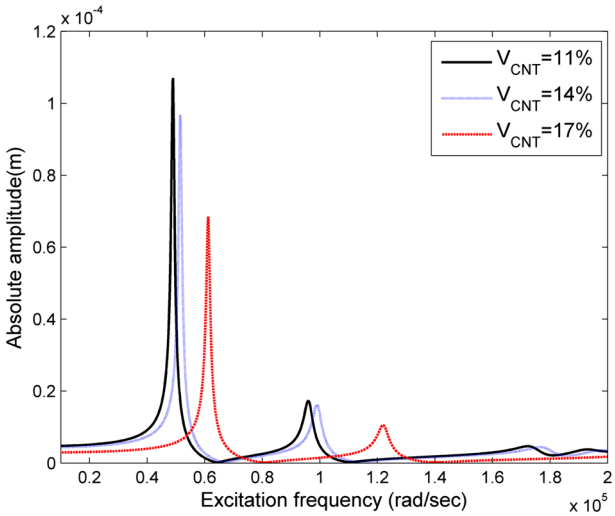

Fig. 8 Absolute amplitude with excitation frequency considering $R/a = 5$, $a/h = 10$ and FG-X distribution for various CNT volume fractions

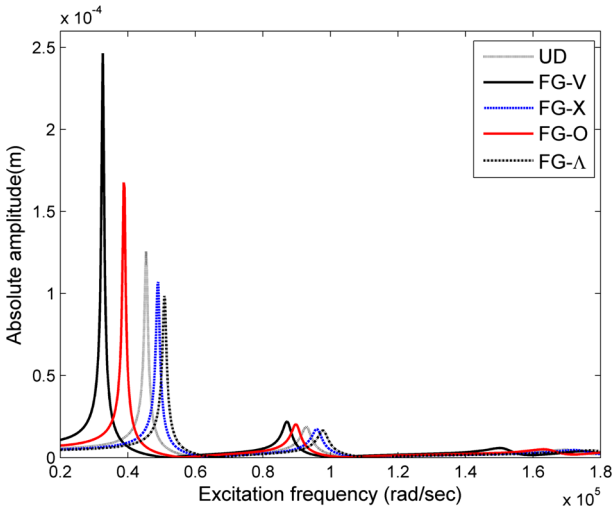

Fig. 9 Absolute amplitude with excitation frequency considering $R/a = 5$, $a/h = 10$ and FG-X distribution for various CNT distributions

with respect to shell geometry (R/a), for FG-X distribution considering different CNT volume fractions of the thin spherical shell structures. From Fig. 10, it is observed that the absolute amplitude drastically decreases with an increase in CNT volume fraction. It can also be seen from Fig. 10 that there is rapid variation of the absolute amplitude with respect to R/a for the deep shell region, and afterward (for shallow to plate region) it has almost negligible variation of the absolute magnitude. So it is cleared from Fig. 10 that the variation of the carbon nanotube volume fraction has ample effect on the absolute amplitude and the corresponding resonant frequency. Figure 11 depicts the variation of the absolute amplitude with respect to R/a, for several CNT distributions considering 11 % CNT volume fraction for a thin shell. From Fig. 11, it is observed that the absolute displacement has more variation in the deep shell region and it has less variation for an other region (i.e., shallow shell and plate). Figure 11 also reveals that various CNT distributions have significant effect on absolute displacement; specifically FG-V and FG-Λ distributions attain the highest and lowest value of absolute displacement, respectively. It is also clearly observed from Figs. 8, 9, 10 and 11 that the absolute amplitude of frequency response decreases with inclusions of CNTs, and the best CNT distribution is FG-Λ which gives the least absolute amplitude and more resonant frequency compared to the other CNT distributions considered.

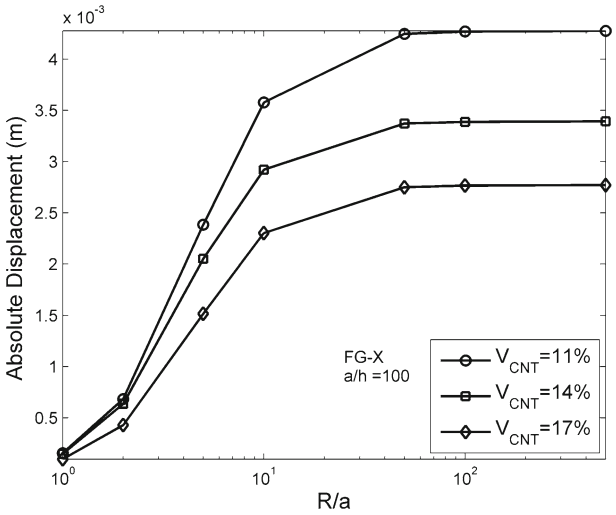

Fig. 10 Absolute amplitude with R/a ratio considering $a/h = 100$ and FG-X distribution for various CNT volume fractions

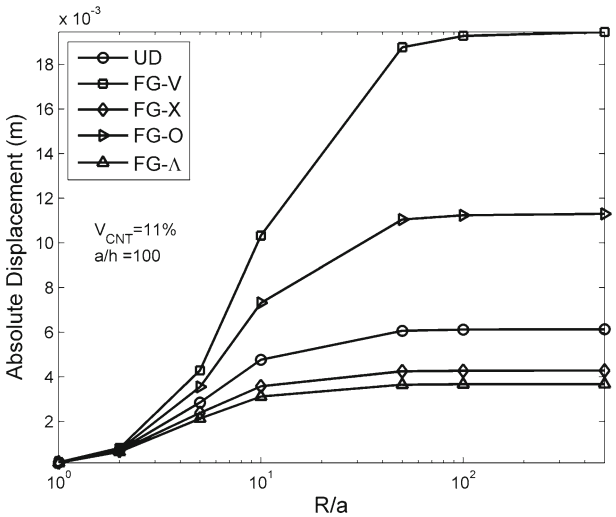

Fig. 11 Absolute amplitude with R/a ratio considering $a/h = 100$ and $V_{\text{cnt}} = 11\ \%$ for various CNT distributions

3.4 Comparative study of different types of FG shell structures

For the comparative study, various types of simply supported FG shell structures on the square base ($a = b$) such as ellipsoidal ($R_1 = 1.5R_2$), doubly curved ($R_1 = 2R_2$), spherical ($R_1 = 1.5R_2$), and cylindrical ($R_2 = 1.5R_2$) have been analyzed for impulse and frequency responses in terms of settling time, first resonant frequency and absolute amplitude corresponding to the resonant frequency. The thicknesses of these shells are considered the same as the spherical shell structure. Table 5 represents the comparison of settling times for various types of shell structures considering different volume fractions of CNTs for a particular type of shell ($R/a = 5$, $a/h = 10$ and 100). It is observed from Table 5 that the settling time required for the impulse response is more in case of a cylindrical shell than that of the other types of shells considered, whereas it is least in case of a doubly curved shell as it is stiffer than other types of shell. It has also been observed from Table 5 that settling times for the impulse responses of the above four types of shell decrease as the volume fraction of CNT increases. The comparative study of the first resonant frequency and the absolute amplitude corresponding to the first resonant frequency of various types of shell structures is also presented in Table 6. From Table 6, it is observed that the maximum value of the first resonant frequency and minimum value of the absolute amplitude corresponding to the first resonant frequency occur for a doubly curved shell as it is stiffer than the other type of shell. It has also been observed from Table 6 that for all types of shell the first resonant

Table 5 Settling time variation for different types of shell (for FG-X distribution)

$V_{cnt}(\%)$	a/h	R/a	Settling time in seconds ($\times 10^{-3}$ s)			
			Spherical	Cylindrical	Ellipsoidal	Doubly curved
11	10	5	1.0460	1.0457	1.0417	1.0391
		10	1.0416	1.0415	1.0406	1.0400
		50	1.0402	1.0402	1.0402	1.0402
		100	1.0402	1.0402	1.0402	1.0402
	100	5	48.771	59.692	46.903	43.543
		10	59.496	63.547	58.599	56.812
		50	64.741	64.923	64.695	64.597
		100	64.920	64.963	64.909	64.885
14	10	5	0.9940	0.9935	0.9900	0.9877
		10	0.9896	0.9894	0.9886	0.9880
		50	0.9882	0.9882	0.9881	0.9881
		100	0.9881	0.9881	0.9881	0.9881
	100	5	45.365	54.110	43.775	40.905
		10	53.925	56.994	53.220	51.818
		50	57.867	58.001	57.832	57.759
		100	57.999	58.031	57.991	57.973
17	10	5	0.8365	0.8364	0.8331	0.8309
		10	0.8331	0.8331	0.8323	0.8318
		50	0.8321	0.8321	0.8320	0.8320
		100	0.8320	0.8320	0.8320	0.8320
	100	5	39.159	48.186	37.634	34.894
		10	48.029	51.421	47.284	45.800
		50	52.430	52.584	52.391	52.308
		100	52.582	52.619	52.573	52.552

Table 6 Absolute amplitude and corresponding first resonant frequency for different types of shell

Parameters	V_{cnt} (%)	Type of shell			
		Spherical	Cylindrical	Ellipsoidal	Doubly curved
First resonant frequency (rad/sec)	11	4.9×10^4	4.9×10^4	4.92×10^4	4.92×10^4
	14	5.14×10^4	5.14×10^4	5.16×10^4	5.18×10^4
	17	6.12×10^4	6.12×10^4	6.14×10^4	6.16×10^4
Absolute amplitude corresponding to first resonant frequency (m)	11	10.7×10^{-5}	10.81×10^{-5}	10.61×10^{-5}	10.59×10^{-5}
	14	9.65×10^{-5}	9.68×10^{-5}	9.567×10^{-5}	9.55×10^{-5}
	17	6.854×10^{-5}	6.896×10^{-5}	6.795×10^{-5}	6.707×10^{-5}

For $R/a = 5$, $a/h = 10$ and FG-X distribution

frequency increases and the absolute amplitude corresponding to the first resonant frequency decreases as the volume fraction of CNT increases. From Tables 5 and 6, it has been observed that the settling time decreases and resonant frequency increases for various types of FG shell structures with the inclusion of CNTs in host structures. Thus, the results signify that addition of CNTs increases the damping capacity of the structures.

4 Conclusions

In this article, a vibration analysis of various functionally graded carbon nanotube-reinforced composite (FG-CNTRC) shell structures is performed. The extended rule of mixture is employed to find the effective elastic properties of a SWCNT-reinforced composite laminate. The evaluated material properties have been used to study the impulse and frequency responses of the different types of FG-CNTRC shell structures. In order to examine the effect of different distributions of the CNTs on the dynamic behavior of the FG-CNTRC shell, uniform distribution (UD) and functionally graded distributions (such as FG-X, FG-V, FG-O and FG-Λ) of carbon nanotubes along the thickness direction of the nanocomposite shell have also been considered. An eight-node shell element is employed for finite element discretization of such shell structures. The study reveals that

all the elastic properties of the composite are influenced by the volume fraction of CNTs and CNT distribution. The transient analysis reveals that the settling time of the said structure is predominantly influenced by the SWCNT volume fraction and CNT distributions which imply that the damping capacity of such a composite structure can be improved by the addition of CNTs and by selecting an appropriate distribution. So, there is a significant effect of addition of SWCNT in vibration and damping characteristics of the structure.

A frequency response analysis confirms that the system has gained stiffness and damping due to the use of SWCNT in the composite shell. In addition, a comparative study of the impulse and frequency response analysis for different types of shells confirms that addition of CNTs has a significant effect on the damping capacity of the structure.

Further, transient and frequency response analysis also reveals that FG-V and FG-Λ distributions have more prominent effects on the responses as they attain the highest and lowest values of settling time and absolute amplitude, respectively.

Finally, it can be concluded that due to addition of CNTs good vibration and damping characteristic as well as better dynamic behavior of the structure can be achieved by proper grading of distributions of CNTs along the thickness direction of the structure.

Appendix

The matrices associated with Eq. (37) are given below:

$$[\rho] = \sum_{k=1}^{n} \int_{z_k}^{z_{k+1}} \begin{bmatrix} \rho^k & 0 & 0 & \rho^k z & 0 \\ & \rho^k & 0 & 0 & \rho^k z \\ & & \rho^k & 0 & 0 \\ & & & \rho^k z^2 & 0 \\ & & & & \rho^k z^2 \end{bmatrix},$$

$$[N] = \begin{bmatrix} N_1 & 0 & 0 & 0 & 0 & \dots & N_n & 0 & 0 & 0 & 0 \\ 0 & N_1 & 0 & 0 & 0 & \dots & 0 & N_n & 0 & 0 & 0 \\ 0 & 0 & N_1 & 0 & 0 & \dots & 0 & 0 & N_n & 0 & 0 \\ 0 & 0 & 0 & N_1 & 0 & \dots & 0 & 0 & 0 & N_n & 0 \\ 0 & 0 & 0 & 0 & N_1 & \dots & 0 & 0 & 0 & 0 & N_n \end{bmatrix}$$

where the shape functions of the eight-node serendipity element are:

$$\begin{aligned} N_1 &= \tfrac{1}{4}(1-\xi)(1-\eta)(-1-\xi-\eta); & N_2 &= \tfrac{1}{2}(1-\xi^2)(1-\eta); \\ N_3 &= \tfrac{1}{4}(1+\xi)(1-\eta)(-1+\xi-\eta); & N_4 &= \tfrac{1}{2}(1+\xi)(1-\eta^2); \\ N_5 &= \tfrac{1}{4}(1+\xi)(1+\eta)(-1+\xi+\eta); & N_6 &= \tfrac{1}{2}(1-\xi^2)(1+\eta); \\ N_7 &= \tfrac{1}{4}(1-\xi)(1+\eta)(-1-\xi+\eta); & N_8 &= \tfrac{1}{2}(1-\xi)(1-\eta^2). \end{aligned}$$

Here, ρ^k is the volumetric density at the kth layer.

The various submatrices of Eq. (39) are given as below:

$$\left[B_u^e\right] = \begin{bmatrix} B_b^e & 0 \\ 0 & B_s^e \end{bmatrix},$$

$$C = \begin{bmatrix} D_b & 0 \\ 0 & D_s \end{bmatrix} = \begin{bmatrix} A & B & 0 \\ B & D & 0 \\ 0 & 0 & A_s \end{bmatrix} = \begin{bmatrix} A_{11} & A_{12} & A_{16} & B_{11} & B_{12} & B_{16} & 0 & 0 \\ A_{12} & A_{22} & A_{26} & B_{12} & B_{22} & B_{26} & 0 & 0 \\ A_{16} & A_{26} & A_{66} & B_{16} & B_{26} & B_{66} & 0 & 0 \\ B_{11} & B_{12} & B_{16} & D_{11} & D_{12} & D_{16} & 0 & 0 \\ B_{12} & B_{22} & B_{26} & D_{12} & D_{22} & D_{26} & 0 & 0 \\ B_{16} & B_{26} & B_{66} & D_{16} & D_{26} & D_{66} & 0 & 0 \\ 0 & 0 & 0 & 0 & 0 & 0 & A_{44} & A_{45} \\ 0 & 0 & 0 & 0 & 0 & 0 & A_{45} & A_{55} \end{bmatrix},$$

References

1. Iijima, S.: Helical microtubules of graphitic carbon. Nature **354**, 56–58 (1991)
2. Thostenson, E.T., Ren, Z.F., Chou, T.W.: Advances in the science and technology of carbon nanotubes and their composites: a review. Compos. Sci. Technol. **61**, 1899–1912 (2001)
3. Dai, H.: Carbon nanotubes: opportunities and challenges. Surf. Sci. **500**, 218–241 (2002)
4. Fidelus, J.D., Wiesel, E., Gojny, F.H., Schulte, K., Wagner, H.D.: Thermo-mechanical properties of randomly oriented carbon/epoxy nanocomposites. Compos. Part A **36**, 1555–1561 (2005)
5. Han, Y., Elliott, J.: Molecular dynamics simulations of the elastic properties of polymer/carbon nanotube composites. Comput. Mater. Sci. **39**, 315–323 (2007)
6. Zhu, R., Pan, E., Roy, A.K.: Molecular dynamics study of the stress–strain behaviour of carbon-nanotube reinforced Epon 862 composites. Mater. Sci. Eng. A **447**, 51–57 (2007)
7. Odegard, G.M., Gates, T.S., Wise, K.E., Park, C., Siochi, E.J.: Constitutive modelling of nanotube-reinforced polymer composites. Compos. Sci. Technol. **63**, 1671–1687 (2003)
8. Shi, D.-L., Feng, X.-Q., Huang, Y. Y., Hwang, K.-C., Gao, H.: The effect of nanotube waviness and agglomeration on the elastic property of carbon nanotube reinforced composites. J. Eng. Mater. Technol. **126**, 250–257 (2004)
9. Wuite, J., Adali, S.: Deflection and stress behaviour of nanocomposite reinforced beams using a multiscale analysis. Compos. Struct. **71**, 388–396 (2005)
10. Shen, H.S., Zhang, C.L.: Thermal buckling and postbuckling behavior of functionally graded carbon nanotube-reinforced composite plates. Mater. Des. **31**, 3403–3411 (2010)
11. Shen, H.S.: Nonlinear bending of functionally graded carbon nanotube reinforced composite plates in thermal environments. Compos. Struct. **91**, 9–19 (2009)
12. Shen, H.S.: Postbuckling of nanotube–reinforced composite cylindrical shells in thermal environments, Part I: axially-loaded shells. Compos. Struct. **93**, 2096–2108 (2011)
13. Zhu, P., Lei, Z.X., Liew, K.M.: Static and free vibration analyses of carbon nanotube–reinforced composite plates using finite element method with first order shear deformation plate theory. Compos. Struct. **94**, 1450–1460 (2012)
14. Yas, M.H., Heshmati, M.: Dynamic analysis of functionally graded nanocomposite beams reinforced by randomly oriented carbon nanotube under the action of moving load. Appl. Math. Model. **36**, 1371–1394 (2012)
15. Aragh, B.S., Barati, A.H.N., Hedayati, H.: Eshelby–Mori–Tanaka approach for vibrational behavior of continuously graded carbon nanotube-reinforced cylindrical panels. Compos. Part B **43**, 1943–1954 (2012)
16. Moradi-Dastjerdi, R., Pourasghar, A., Foroutan, M., Bidram, M.: Vibration analysis of functionally graded nanocomposite cylinders reinforced by wavy carbon nanotube based on mesh-free method. J. Compos. Mater. **48**, 1901–1913 (2014)
17. Zhang, L.W., Lei, Z.X., Liew, K.M., Yu, J.L.: Static and dynamic of carbon nanotube reinforced functionally graded cylindrical panels. Compos. Struct. **111**, 205–212 (2014)
18. Liew, K.M., Lei, Z.X., Zhang, L.W.: Mechanical analysis of functionally graded carbon nanotube reinforced composites: a review. Compos. Struct. **120**, 90–97 (2015)
19. Zhang, L.W., Lei, Z.X., Liew, K.M.: Vibration characteristic of moderately thick functionally graded carbon nanotube reinforced composite skew plates. Compos. Struct. **122**, 172–183 (2015)
20. Zhang, L.W., Lei, Z.X., Liew, K.M.: Free vibration analysis of functionally graded carbon nanotube-reinforced composite triangular plates using the FSDT and element-free IMLS-Ritz method. Compos. Struct. **120**, 189–199 (2015)
21. Zhang, L.W., Lei, Z.X., Liew, K.M.: Buckling analysis of FG-CNT reinforced composite thick skew plates using an element-free approach. Compos. Part B **75**, 36–46 (2015)
22. Phung-Van, P., Abdel-Wahab, M., Liew, K.M., Bordas, S.P.A., Nguyen-Xuan, H.: Isogeometric analysis of functionally graded carbon nanotube-reinforced composite plates using higher-order shear deformation theory. Compos. Struct. **123**, 137–149 (2015)
23. Alibeigloo, A., Emtehani, A.: Static and free vibration analyses of carbon nanotube reinforced composite plate using differential quadrature method. Meccanica **50**, 61–76 (2015)
24. Kundalwal, S.I., Meguid, S.A.: Effect of carbon nanotube waviness on active damping of laminated hybrid composite shells. Acta Mech. **226**, 2035–2052 (2015)
25. Zeighampour, H., Beni, Y.T., Mehralian, F.: A shear deformable conical shell formulation in the framework of couple stress theory. Acta Mech. **226**, 2607–2629 (2015)
26. Weng, G.J.: Effective bulk moduli of two functionally graded composites. Acta Mech. **166**, 57–67 (2003)
27. Alian, A.R., Kundalwal, S.I., Meguid, S.A.: Multiscale modeling of carbon nanotube epoxy composites. Polymer **70**, 149–160 (2015)
28. Kumar, R.S., Ray, M.C.: Active control of geometrically nonlinear vibrations of doubly curved smart sandwich shells using 1–3 piezoelectric composites. Compos. Struct. **105**, 173–187 (2013)
29. Kundalwal, S.I., Suresh Kumar, R., Ray, M.C.: Smart damping of laminated fuzzy fiber reinforced composite shells using 1–3 piezoelectric composites. Smart Mater. Struct. **22**, 105001 (2013). doi:10.1088/0964-1726/22/10/105001
30. Koiter W.T.: A consistent first approximation of the general theory of thin elastic shell. In: Proceedings of First IUTAM Symposium, North-Holland, Amsterdam, pp. 12–33 (1960)
31. Sk, L., Sinha, P.K.: Improved finite element analysis of multilayered doubly curved composite shells. J. Reinf. Plast. Compos. **24**, 385–404 (2005)
32. Roy, T., Manikandan, P., Chakraborty, D.: Improved shell finite element for piezothermoelastic analysis of smart fiber reinforced composite structures. Finite Elem. Anal. Des. **46**, 710–720 (2010)
33. Wempner, G., Talaslidis, D.: Mechanics of Solids and Shells. CRC Press, Boca Raton, FL (2003)
34. Chowdhury, I., Dasgupta, S.P.: Computation of Rayleigh damping coefficients for large systems. EJGE **8C**, 1–11 (2003)
35. Wang, C.Y., Zhang, L.C.: A critical assessment of the elastic properties and effective wall thickness of single-walled carbon nanotubes. Nanotechnology **19**, 075075 (2008)